Electronic Supplementary Material (ESI) for Lab on a Chip.

Supplementary Information

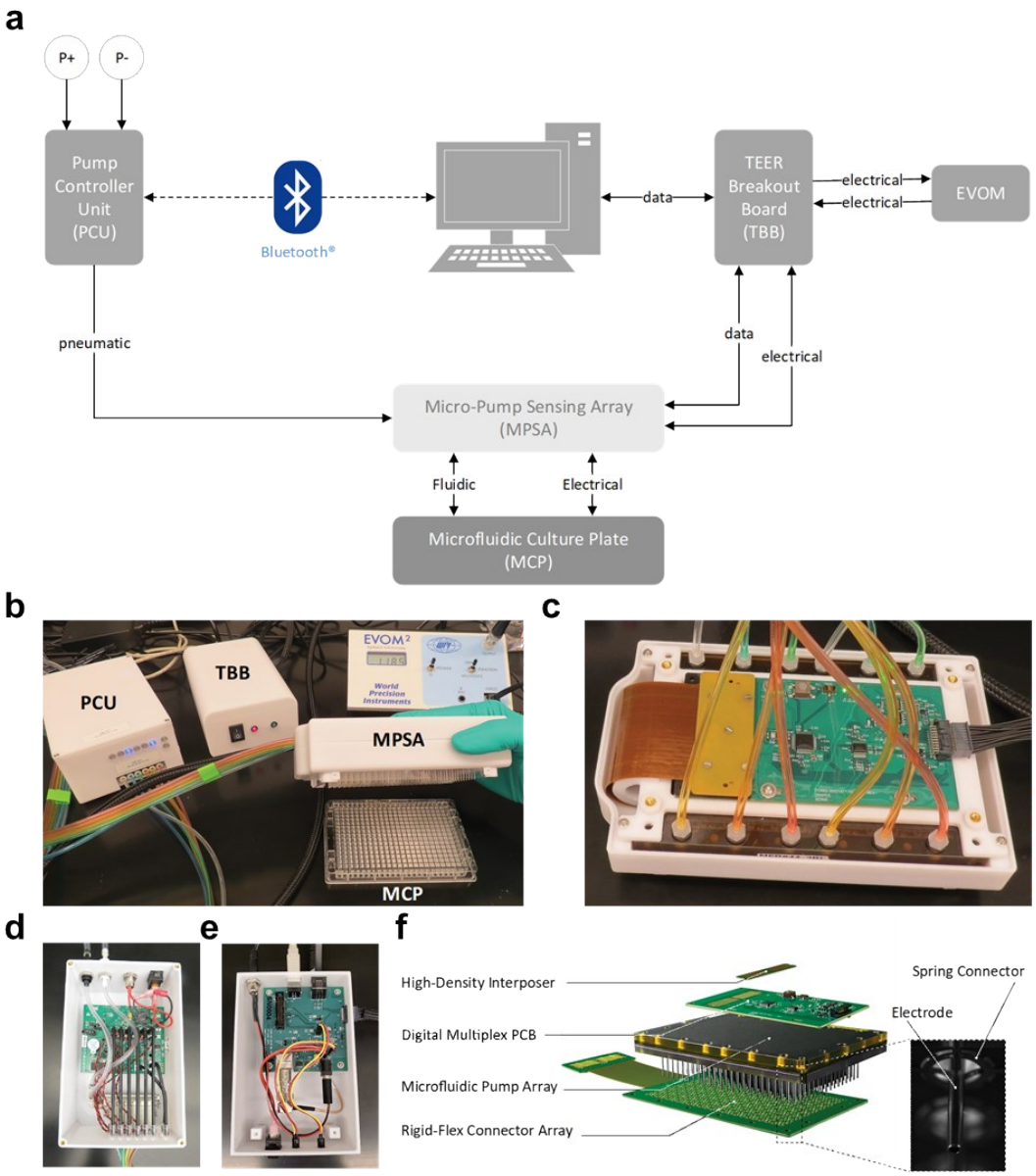

Supplementary Fig. 1 | Integrated micro-pump sensing array (MPSA) provides perfusion and sensing capabilities in a high throughput format. a, System block diagram for the organ-on-chip platform. **b**, Micro-pump sensing array is connected to the system control components. Pump control unit (PCU) pneumatically controls the pump array while the TEER breakout board (TBB) provides the necessary connections between the sensing array of MPSA, personal computer, and the auxiliary measurement system (here EVOM**). c**, Assembled MPSA system in its enclosure. **d**, View of the PCU and its components. **e**, View of the TBB and its components. **f**, Exploded view photographs of the MPSA comprising the micropump array and the electronics hardware of the sensor array. An array of micro-machined leaf spring connectors (inset) electrically couple the stainless steel tubes of the micropump array to a digital multiplex printed circuit board through a rigid-flex routing board. This allows the tubes of the micropump array to function as electrodes. The board is connected using a high density interposer. The rigid portion of the rigid-flex connector array is inserted onto the micropump array, while the flex portion folds back on top of the micropump array to make electrical connections to the digital multiplex board. The assembled MPSA is subsequently encased in a protective enclosure.

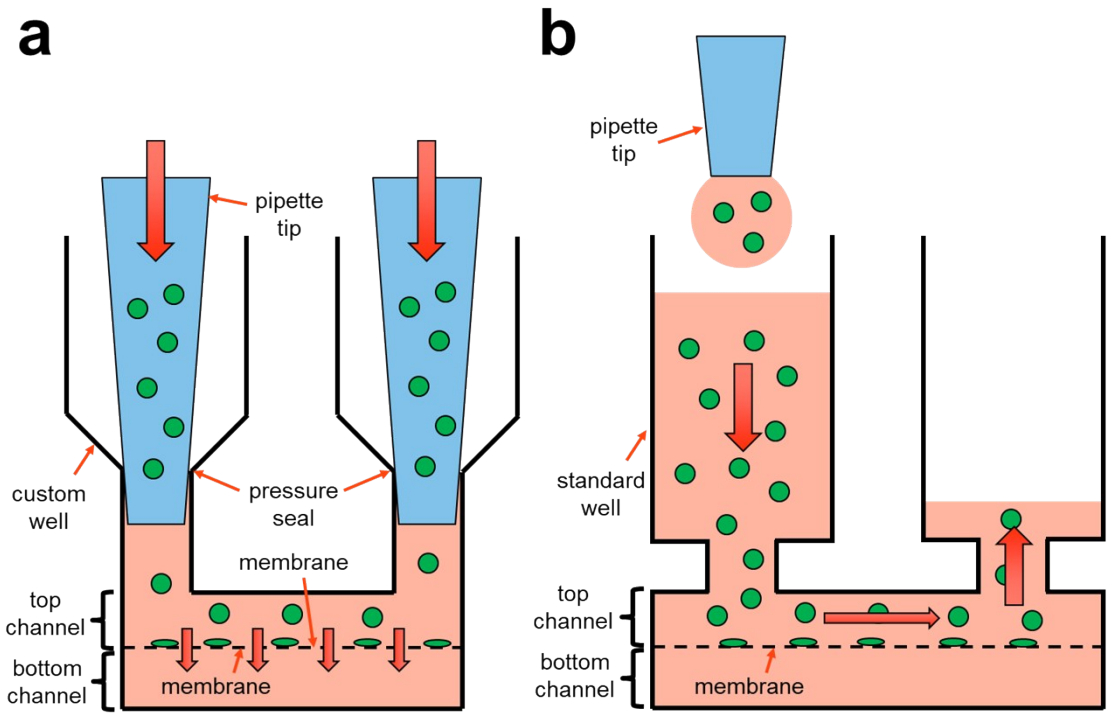

Supplementary Fig. 2 | Seeding Methods. a, "filter seeding": two pipette tips are inserted into the two wells of the top channel of a single device of a custom well plate such that the tips make pressure seals with the angled bottoms of the wells. Once seated, cell suspension is pipetted simultaneously from both pipettes forcing the liquid across the membrane into the bottom channel while the cells are collected on the membrane where they will adhere and spread. This process can also be performed in the bottom channel to seed cells onto the bottom side of the membrane. **b**, "gravity seeding": cell suspension in pipetted into a single channel of a device. The pressure head created by this addition of fluid drives the suspension through the channel and into well at the other end of the channel. Cells settle onto the membrane under the influence of gravity where they adhere and spread.

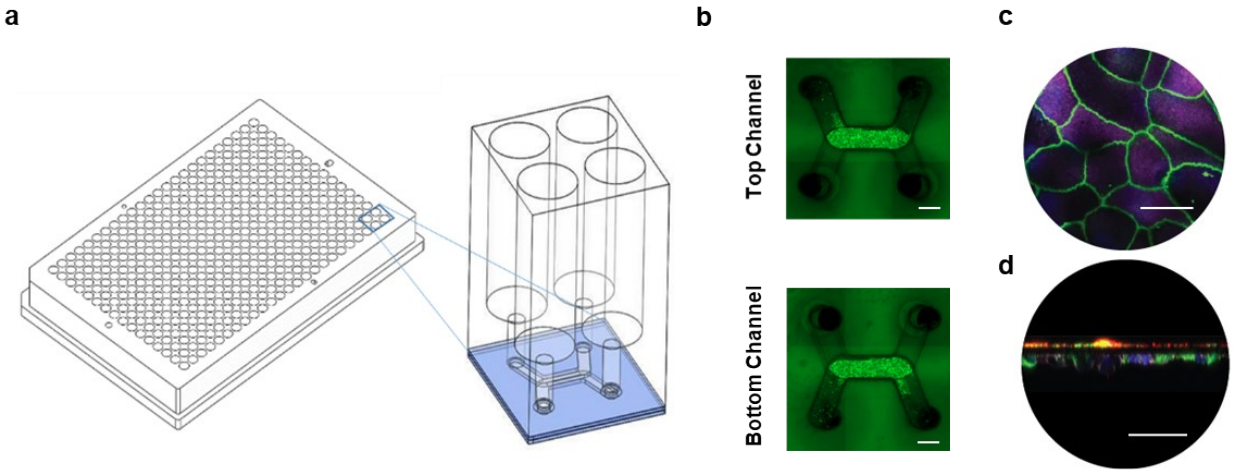

Supplementary Fig. 3 | Custom configuration of the microfluidic culture plate. a, Reservoir geometry allows a liquid tight seal between the channel ports and pipette tips, facilitating a flow-assisted cell seeding and retrieval of cells and genetic material. **b**, Simultaneous introduction of the cell suspension at the inlet and outlet ports of the microfluidic culture device concentrates the cells to the overlap region of the device and enables apical (top channel) or basal (bottom channel) seeding of the cells onto the microporous scaffold. Here colon cells are used. Scale bar represents 1 mm. **c**, High magnification confocal microscopy of the cultured colon cells. Scale bar represents 20 µm. **d**, Confocal orthogonal projection of the renal proximal tubule model showing co-culture of human primary renal proximal tubule epithelial cells and human primary microvascular cells on either side of the membrane. Scale bar represents 50 µm.

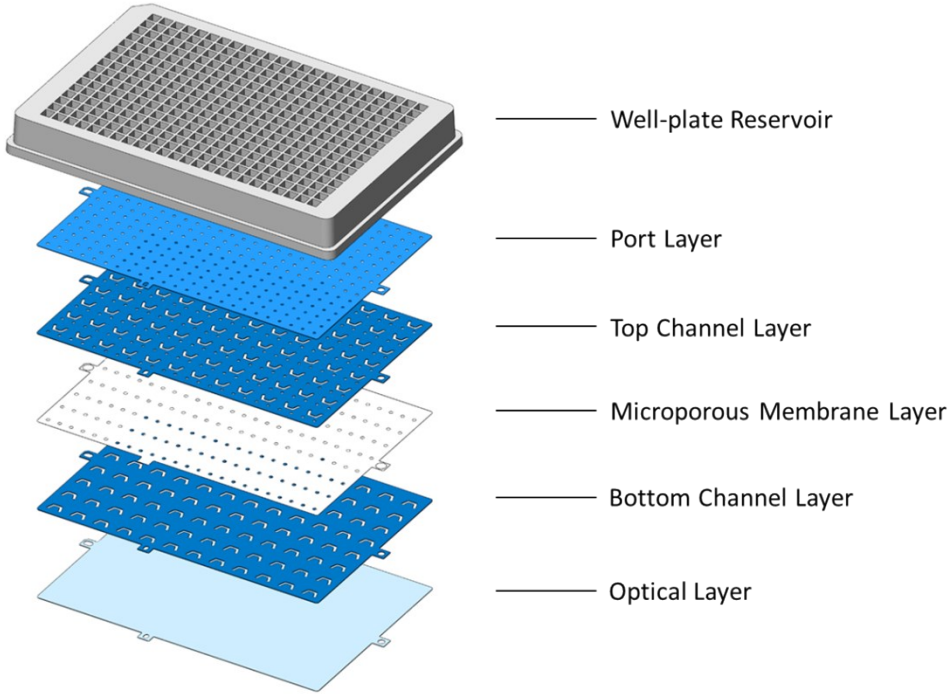

Supplementary Fig. 4 | Exploded view of the multi-layer microfluidic culture plate.

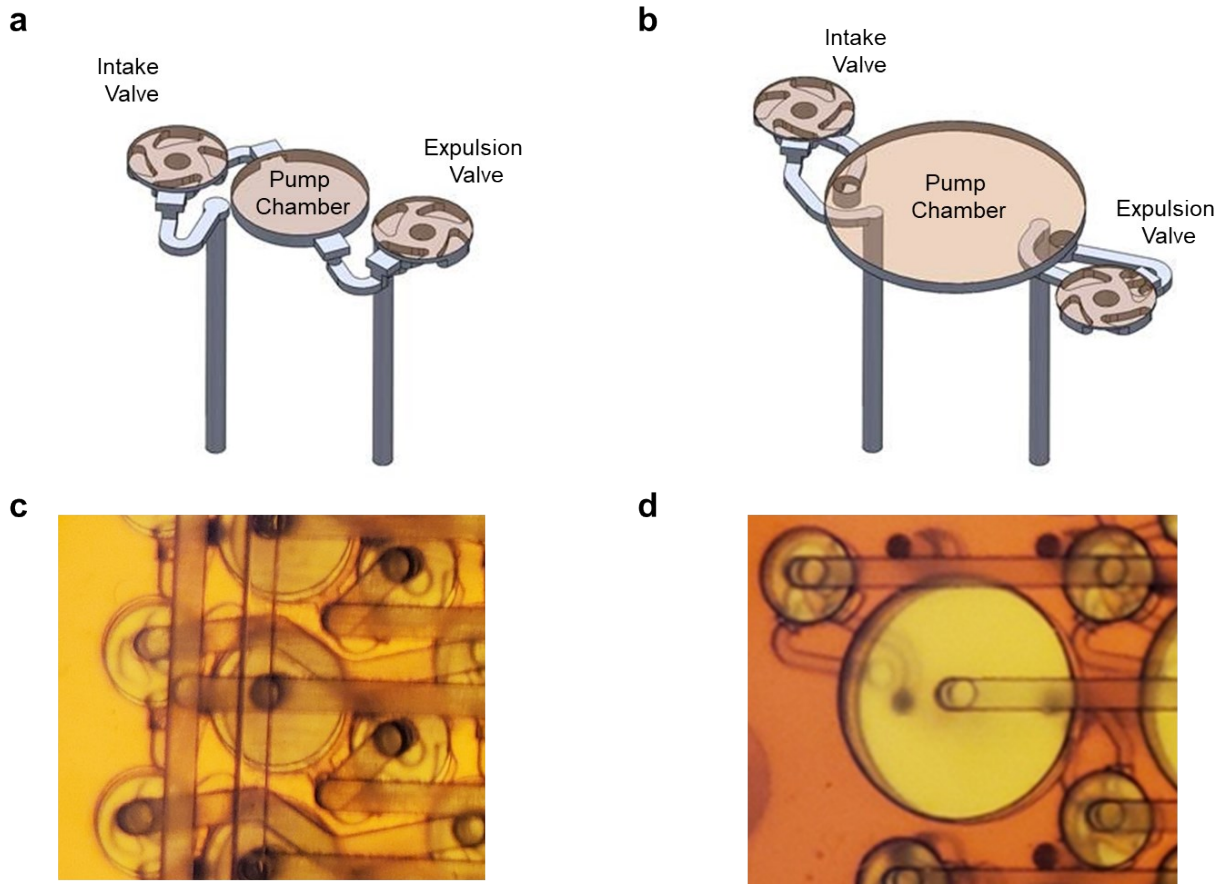

Supplementary Fig. 5 | Fluidic circuit for microfluidic pumps. Each individual microfluidic pump is comprised of a fluidic circuit and a pneumatic manifold. The fluidic circuit of each pump is made up of a pump chamber with two valves at the upstream and downstream positions and was separated from the pneumatic manifold by a thin polyimide membrane. **a**, The fluidic path of the standard 1.3 µL-stroke-volume micropump with a prime volume of 18.4 µL. **b**, The fluidic path of the high shear 12 µL-stroke-volume micropump with a prime volume of 26.4 µL. **c**, and **d**, Close-up view of the pump chamber and valve assembly for the assembled microfluidic pumps. The images include the pneumatic channels addressing pump chambers and valves.

Fabrication of the microfluidic culture plates. Microchannels were laser cut (Resonetics, Nashua, NH, USA) from composite films of 188 µm-thick cyclic olefin polymer (ZF14-188: Zeon Corp., Tokyo, Japan) and 28 µm-thick cyclic olefin copolymer (8007 COC: Tekni-plex, Wayne, PA, USA) laminated in a heated hydraulic press (Carver Inc., Wabash, IN, USA) at 120°C and 1 MPa for 30 minutes. The thin COC layer had a glass transition temperature (T_g) of 78 °C that was below the lamination temperature (120°C) and reflowed during the lamination cycle, facilitating the bonding of the channel layers to the adjacent layers, while the core COP layer had a T_g of 137°C and remained dimensionally stable. Top and bottom microchannel layers were thermally laminated to port and optical layers, respectively, using the above process in a custom alignment fixture. The optical layer consisted of either a 188 µm thick film of COP or a 125 µm thick film of fluorinated ethylene propylene (FEP 500A: American Durafilm, Holliston, MA, USA) depending on the microfluidic culture plate variant. A 22 µm track-etched polycarbonate membrane with pore diameter of 3 µm (it4ip S.A., Louvain-la-Neuve, Belgium) was patterned using an UV laser system (Protolaser U4: LPKF Laser and Electronics, Garbsen, Germany) with an array of via

holes coincident with the inlet and outlet ports of the bottom channel and thermally laminated to the top-port layer composite. The membrane was laminated between the top and bottom microchannel layers using the above lamination process. The composite optical and bottom channel layers was laminated to the entire assembly to complete the microfluidic stack which was subsequently bonded onto the bottom of a custom or standard bottomless 384-well plate (Aurora Microplates, Whitefish, MT, USA).

Fabrication of the micropump array. The micropump array was assembled from a pneumatic manifold layer used to route positive and negative pressure to individual valves and pumps and a fluidic micropump layer (Supplementary Fig. 6). The pneumatic manifold layer was constructed with 4.8 mm Ultem polyetherimide sheets (Boedeker Plastics, Shiner, TX, USA) machined with ports for pneumatic connections and laser micromachined (LPKF Protolaser U4) 0.25 mm thick Ultem sheets (McMaster-Carr, Elmhurst, Illinois USA) coated with a 12.5 µm thick film of phenolic butyral thermosetting adhesive (R/flex 1000, Rogers Corp., Chandler, Arizona, USA). The Ultem components of the pneumatic manifold layer were assembled onto a custom alignment fixture and bonded at 175˚C at a pressure of 1.3 MPa for 1 hour in a heated Carver press. The fluidic micropump layer included a 0.25 mm thick Viton™ fluoroelastomer (AAA ACME Rubber Co., Tempe, AZ, USA) valve seat selectively metalized with a 200 Å layer of titanium using a sputtering system (KDF 954ix: KDF Electronic & Vacuum Services Inc., Rockleigh, NJ, USA) and laser micromachined. Fluidic micropump layer components were laser micromachined from Ultem using the same process as the pneumatic manifold layer. The pneumatic manifold and the fluidic micropump layer were assembled and thermally laminated along with a pre-tensioned 25 µm Kapton membrane (Fralock, Valencia, CA, USA) separating the two and laser-cut 50 µm and 125 µm Kapton stand-off layers coated with adhesive on both sides. Inlet and outlet port tubes (21G 316L stainless steel hypodermic tubes: New England Small Tube Corp., Litchfield, NH, USA) were assembled into the fluidic micropump layer, glued with 353NDPK Hi-Temp Epoxy (Thorlabs, Newton, NJ, USA) and cured at 75˚C overnight. An adapter for positioning the MPSA system onto the microfluidic culture plates was made via 3D-printed fused deposition of polycarbonate (Fortus 400mc, Stratasys, Eden Prairie, MN, USA) with viewing panels machined from clear polycarbonate. Micropumps are evaluated for flow rates and ability to pump to rule out any defective pumps.

Integration of TEER sensors. The submerged electrodes were electrically coupled to the external measurement system using a custom connector array made up of an 8-layer rigid-flex printed circuit board (PCB) soldered to an array of 384 laser micro-machined stainless steel leaf spring connectors. The rigid-flex PCB was connected to a 10 layer digital multiplex PCB containing 12 32-channel multiplex switches and the microcontroller unit (STM32L0: STMicroelectronics, Geneva, Switzerland), through a high-density interposer (Z-Ray: Samtec, New Albany, IN, USA). The MCU's built-in analog-to-digital converter (ADC) sampled the analog output voltage of an external measurement device (EVOM2: World Precision Instruments, Sarasota, FL, USA), and the data was buffered before being streamed to a host computer using a serial communication protocol through a Universal Asynchronous Receiver/Transmitter chip (FTDI, Glasgow, Scotland). The integrated MPSA system was assembled in a custom 3D-printed enclosure. The experimental set-up was controlled through a graphical user interface implemented in Python.

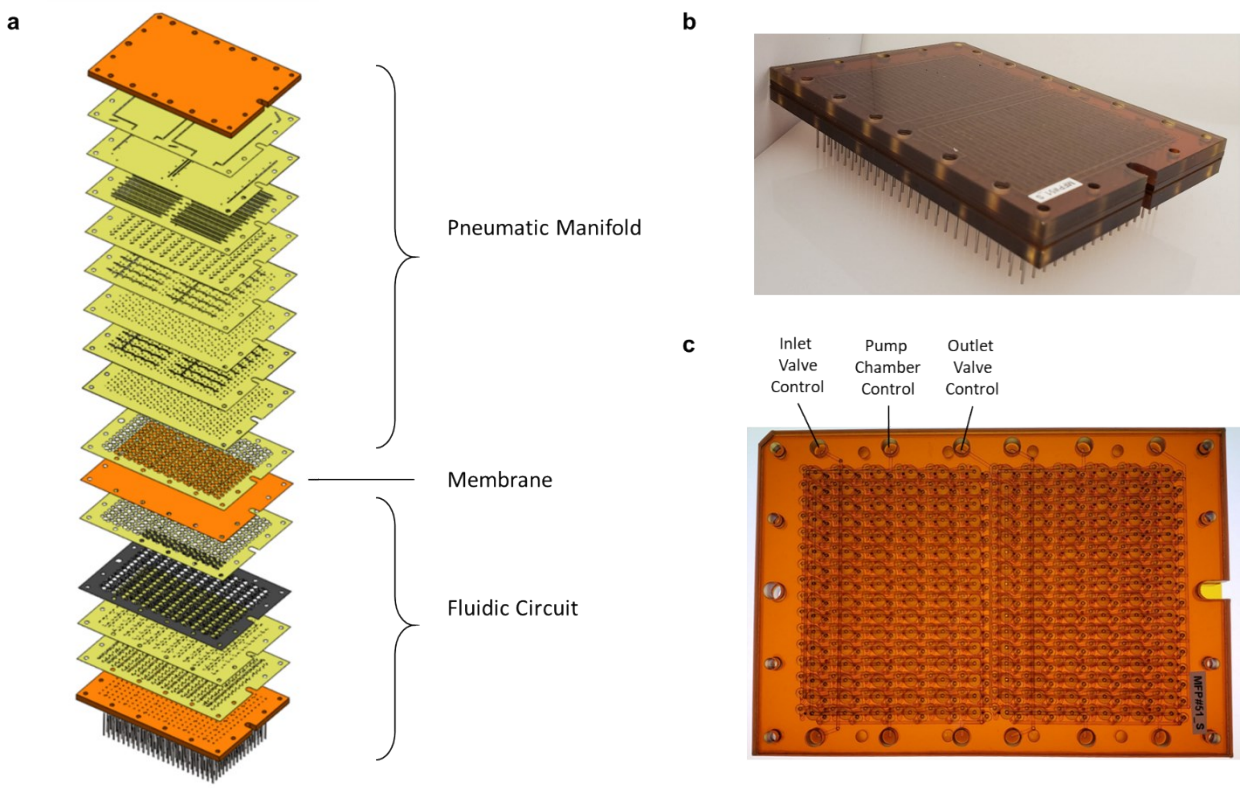

Supplementary Fig. 6 | Micropump array layers and assembly. a, Exploded view of the microfluidic layers comprising the pump assembly. **b**, **c**, Isometric and top view of the assembled micropump array with 192 pneumatically controlled microfluidic pumps.

Micropump principle of operation. The micropumps of the micropump-sensor array (MPSA) are positive displacement pumps and are each comprised of an intake valve, a pump chamber and an expulsion valve (Supplementary Fig. 5), which are all independently actuated by the application of pressure (closed) or vacuum (open) to a thin membrane that covers the tops of the valves/pump chambers. A six-step sequence of openings and closings is used to transfer a bolus of fluid from the inlet to the outlet of the micropump structure (Supplementary Fig. 7). The precise timing of the steps is controlled by the system control (SCU) and is defined by the user via a graphical user interface. The cycling frequency of these actuation steps sets the flow rate of the pump. The pumps serve to transfer fluid from the outlet of the microchannel to the inlet, resulting in a higher column of liquid at the inlet. The pressure differential generated by the higher column of fluid drives the fluid through the microchannel. The pumps prime themselves by being run while placed on a well plate or MCP filled with cell culture medium. By withdrawing fluid into one tube and dropping it out of the other, generation of bubbles is minimized and generation of bubbles during operation or during the MCP removal and replacement process is exceedingly rare. Since the fluid drops into the well during operation, the well serves as a built in bubble trap. In addition, the MCP surface treatments maximize hydrophilicity to discourage bubble formation. Microchannels are inspected for bubbles after seeding and are either manually purged with a pipettor or are removed from the data set if bubbles cannot be removed.

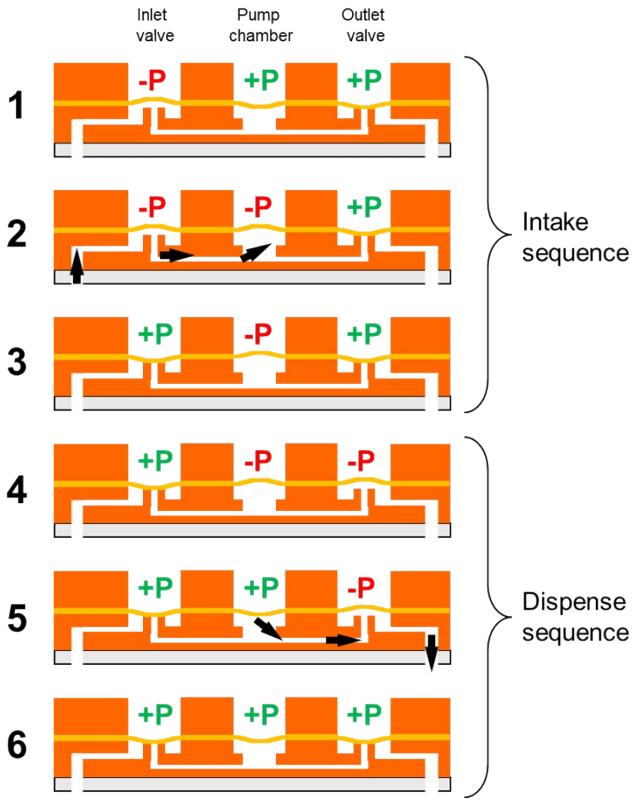

Supplementary Fig. 7 | Micropump array actuation sequence. Sequential application of positive and negative pressure pulses results in the opening and closing of the valves and displacement of the fluid in the pump chambers. Timing of open/closing states are controlled by the SCU and set via a graphical user interface. Here the fluid intake and dispense sequences are depicted. Pump flow rates can be tuned by altering the frequency pneumatic actuation.

Micropump array calibration. To assess the performance of the MPSA micropumps, individual stroke volumes were quantified using a fluorescent-based microplate reader. A black COP 384 well plate (Aurora Microplates, Whitefish, MT, USA) was pre-filled with 100 µL of a 6 µM solution of fluorescein (MilliporeSigma, Burlington, MA, USA) in PBS, as depicted in Supplementary Fig. 8c. The MPSA was placed on the well plate and programmed to pump 50 cycles, or 'strokes', of the solution from one well to the adjacent well, as depicted in Supplementary Fig. 8c. A plate reader (Synergy H1: Biotek, Winooski, VT, USA) was then used to analyse the absorbance of each well with an excitation wavelength of 488 nm and an emission wavelength of 525 nm. The volume in each well was analysed in reference to a volumetric standard, as shown in Supplementary Fig. 8a, which defined a linear fit calibration curve from 10 µL to 100 µL, as shown in Supplementary Fig. 8b. The volume transferred by each micropump was divided by the number of strokes (50) to determine the stroke volume for each micropump. Datasets acquired in this manner were used to calculate average stroke volume, coefficient of variance, and yield of the MPSAs. The average stroke volume was then used to program the flow rate for all experiments. MPSA calibration was conducted immediately after construction and repeated at least once between every experiment.

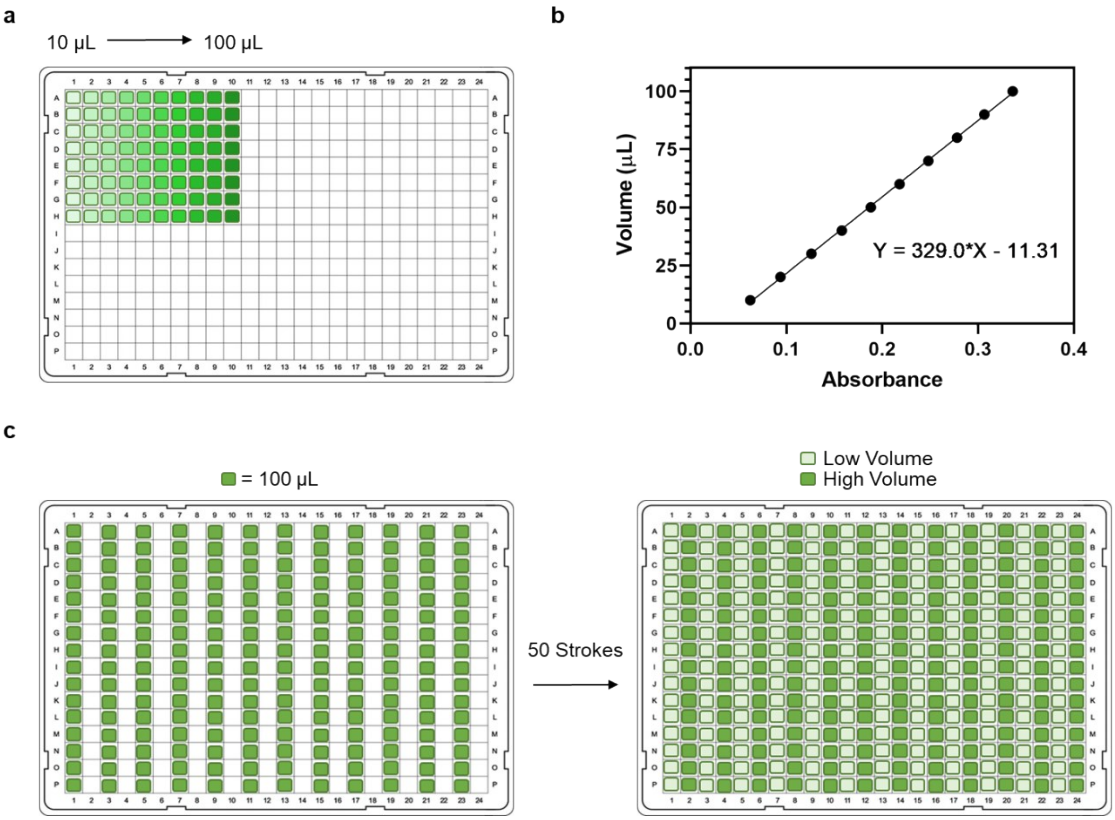

Supplementary Fig. 8| Micropump array calibration procedure. a, **b**, Plate map used for relating the fluid volume in a well to absorbance readout in the plate reader (error bars are within the dot size, R^2=0.9997). **c**, Plate map used for calibration of the micropump array stroke volumes. **d**, After application of a fixed number of strokes (here 50) the absorbance values are used to calculate each micropump's stroke volume.

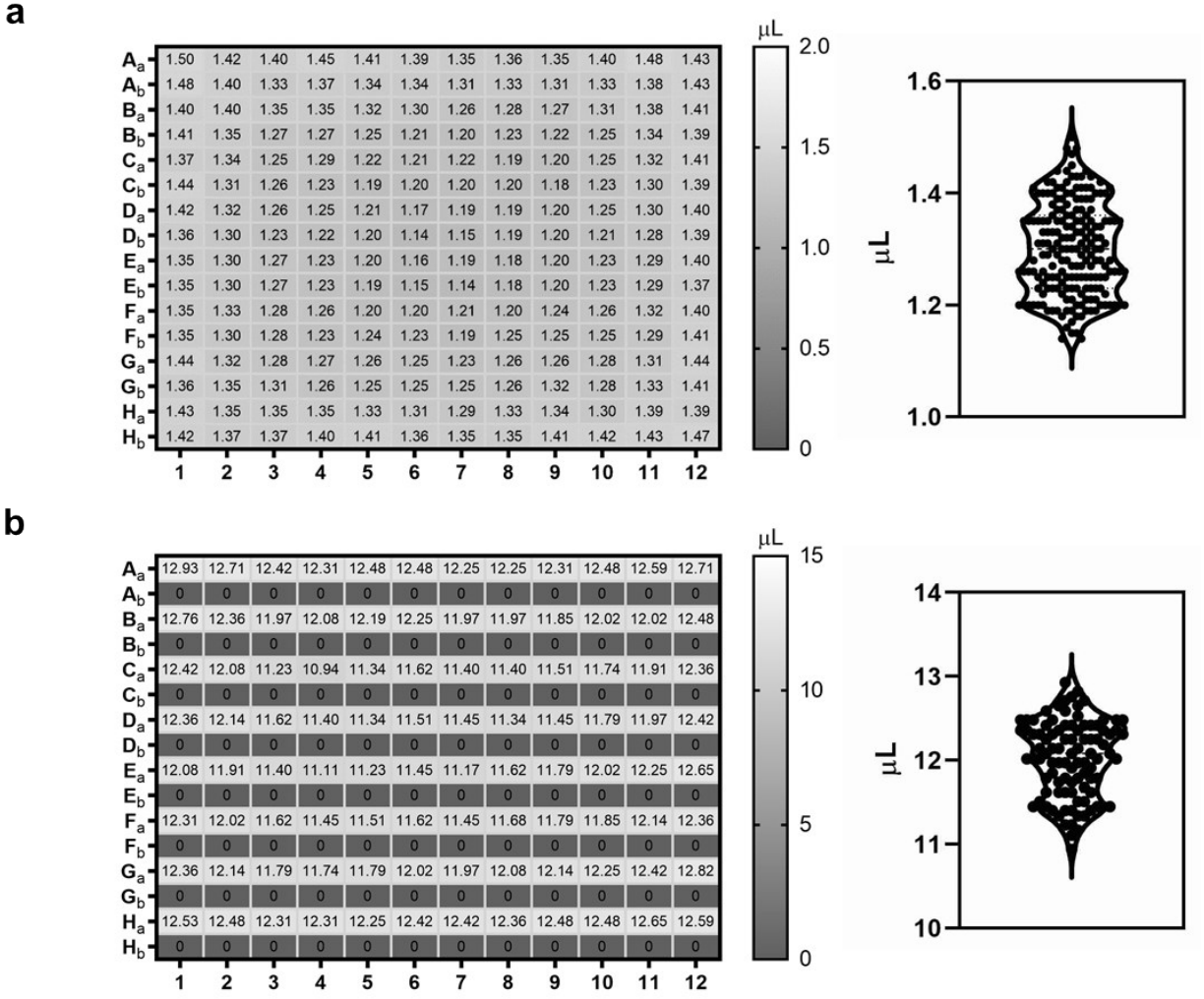

Supplementary Fig. 9 | Micropump array stroke volumes. a, Heat map and violin plot of the stroke volume for each of the 192 microfluidic pumps of the low-shear pump configuration. An average stroke volume of 1.3 ± 0.1 µL is achieved across the all the pumps. Flow rates on the order of 60 µL/min are typically achieved in the platform using this pump configuration. **b**, Heat map and violin plot of the stroke volumes for the 96 microfluidic pumps of the high-shear pump configuration. The average stroke volume of 12 ± 0.5 µL is able to generate flow rates on the order of 700 µL/min in the platform which translates to a wall shear stress of 7.3 dyn/cm^2 in the microfluidic channels of the culture plate.

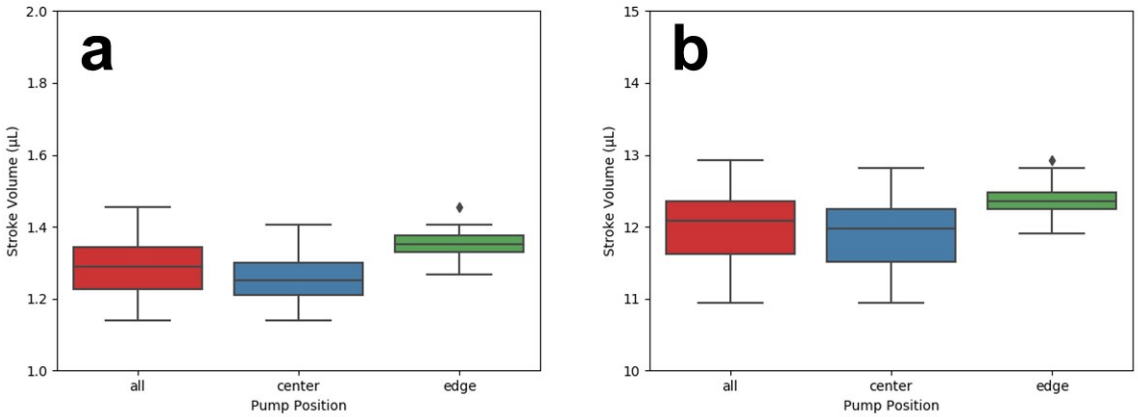

Supplementary Fig. 10 | Micropump stroke volumes by region. Box and whisker plot of the stroke volumes for the micropump of the low shear pump configuration grouped by region (“all”, “center”, “edge”) for **a**. the 192-pump low-shear configuration and **b.** the 96-pump high-shear configuration.

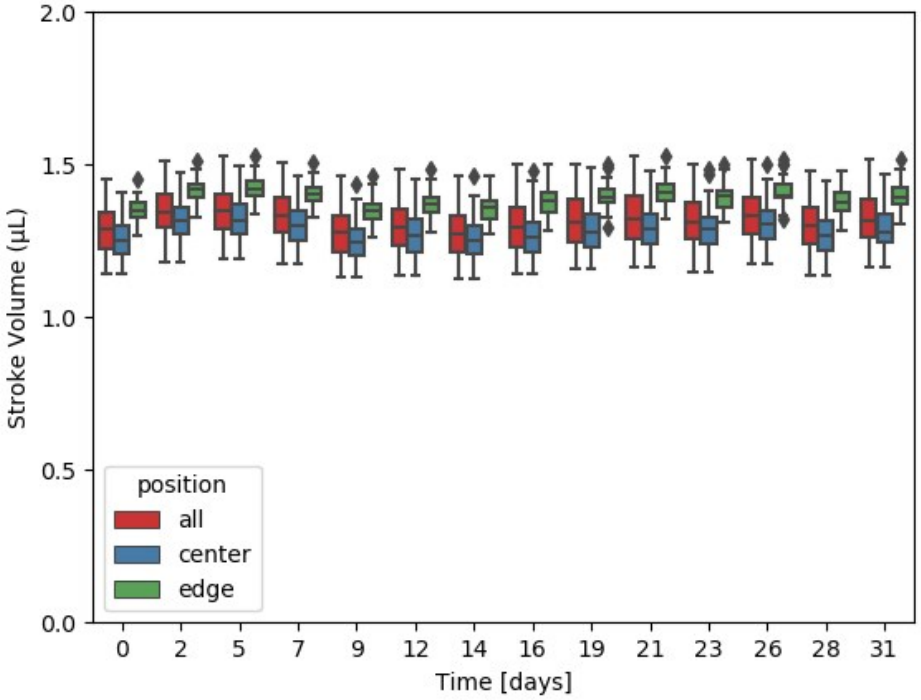

Supplementary Fig. 11 | Micropump array stroke volume stability. Box and whisker plot of recorded stroke volumes across 192 micropumps of the MPSA, measured over 31 days. The red boxes represent data from all 192 micropumps of the MPSA, the green boxes represent the 52 micropumps located at the outer edge of the MPSA ("edge"), and the blue boxes represent the remaining 140 non-edge micropumps ("center"). The black diamonds represent statistical outliers within the group with which they are vertically aligned.

First Order Channel Modeling. In order to select a microfluidic channel geometry to accommodate our design requirements (flow rates, shear stress, number of cells for assays, maximum fluid head height), analytical approximations for gravity driven rectangular duct flow were used to compare predicted performance to the design requirements (Supplementary Fig. 12);

$$u(x,y) = \frac{4h^2}{\mu\pi^3}\left(\frac{dp}{dz}\right)\sum_{i=1,3,5\ldots}^{\infty}\frac{1}{i^3}\left(1-\frac{\cosh\left({}^{i\pi x}/_{h}\right)}{\cosh\left({}^{i\pi w}/_{2h}\right)}\right)\sin\left({}^{i\pi y}/_{h}\right) \quad ,(1)$$

$$Q = \frac{hw^3}{12\mu}\left(-\frac{dp}{dz}\right)\left[1-\frac{192w}{\pi^5 h}\sum_{i=1,3,5\ldots}^{\infty}\left(\frac{\tanh\left({}^{i\pi h}/_{2w}\right)}{i^5}\right)\right] \quad ,(2)$$

where the channel dimensions are given by $-{}^{w}/_{2} \le x \le {}^{w}/_{2}$, $0 \le y \le h$, $u(y,z)$ is the flow field, $\frac{dp}{dz}$ is the pressure gradient in the direction of flow, and μ is the viscosity. The shear stress at the cell layer can be obtained from the derivative of the flow field with respect to y evaluated at $y = 0$, multiplied by viscosity. The pressure was converted into a fluid height to make sure it was below the maximum reservoir height of approximately 12 mm for any particular design. In addition, a required pump rate was estimated by setting a minimum acceptable initial and final fluid flow ratio between pump strokes (here ${}^{Q_f}/_{Q_i} = 0.8$) by using a capacitive discharge model of the fluid flow under gravity. The relevant equations(3) are given by;

$$R = \frac{\Delta P}{Q},$$
$$C = \frac{A}{\rho g},$$
$$t_p = R.C.ln\left(\frac{Q_f}{Qi}\right),$$

where R is the fluidic resistance, ΔP is the pressure drop across the fluid channel (pressure gradient above multiplied by the channel length), Q is the flow rate from equations above, C is the fluid capacitance, A is the reservoir cross-sectional area, ρ is the fluid density, g is gravity constant, Q_f is the final flow rate, Q_i is the initial flow rate and t_p is the time interval where the flow rate decays from the initial to final flow rate. By comparing this time interval to our maximum pumping rate (2 Hz) and stroke volume (here 12 µL), geometries could be evaluated for their feasibility. Once a list of possible geometries were generated, FEA was used to further refine performance predictions.

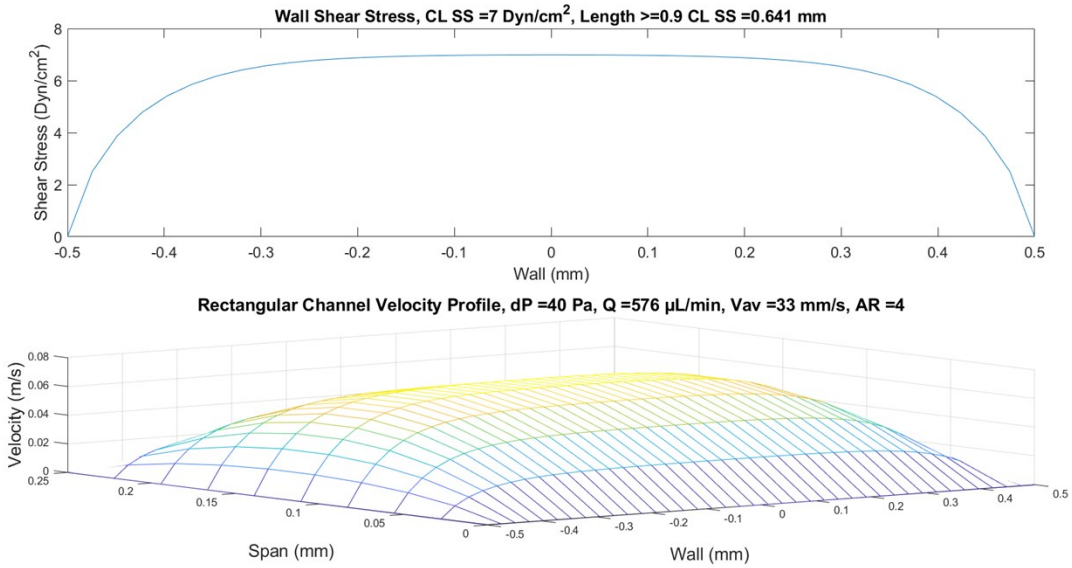

Supplementary Fig. 12 | Shear stress and flow field for rectangular duct flow.

Finite element modelling. Computational modelling was performed using COMSOL Multiphysics software v5.4 (Burlington, MA, USA). To appropriately size the pump chambers for the two different flow regimes generated by the microfluidic pump array, membrane deflections in response to the applied pneumatic pressures were simulated using a 3D finite element model of the solid domain in the Solid Mechanics module. Mechanical properties of the polyimide (Young's modulus, $E = 2.9 \times 10^9$ Pa, and Poisson's ratio, $\nu = 0.34$) were used for the 25 µm Kapton membrane. A fixed boundary condition was imposed on the membrane periphery and symmetry boundaries were utilized in the modelling. Tetrahedral mesh elements were used to discretize the computational domain with physics controlled mesh settings set to extra fine. The surface integral of the membrane deflection under positive and negative applied pressures was used to determine the stroke volume for each pump chamber geometry considered. Simulated results (Supplementary Fig. 13) are in close agreement with experimentally determined strokes volumes for the pumps at the operational pressures of ± 60 kPa (Supplementary Fig. 9).

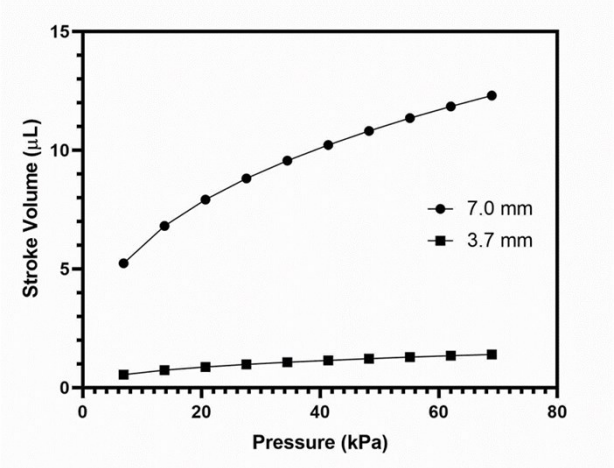

Supplementary Fig. 13 | Finite element simulations of the micropump stroke volumes.

To relate TEER experimental values to actual tissue TEER values in our microfluidic device geometry, a 3D finite element model of the fluid domain of a single device was developed using the Electric Currents module (continuity, Ohms law, field potential). Special consideration is due when evaluating TEER *in vitro*, as it has been shown that dramatic differences can be seen between systems such as Transwells and microfluidic devices(4,5). A stationary approximation (DC TEER) was implemented in order to analyze the electric fields and current. As in the experimental set-up, an electrode pair was fluidically connected to opposite sides of the porous membrane via the reservoirs and microchannels and were assigned as current source and sink (I_+ and I_- respectively) with a constant current between them (10 μA), and a second pair of electrodes connected fluidically to opposite sides of the membrane were used to measure electrical potential (V_+ and V_-). The porous membrane separating the two microchannels in the overlap region was modeled by a spatially uniform contact impedance with an assigned resistance value between 1 to 1000 $\Omega.cm^2$ which represents the algebraic sum of contributions from the membrane and a range of tissue layer resistances. Microscopic effects such as conduction between the cell layer and membrane to a pore and pore distribution were neglected. All other surfaces besides the current carrying electrodes and the porous membrane were set to insulating boundary conditions. Tetrahedral mesh elements were used to discretize the computational domain with physics controlled mesh settings set to extremely fine. The porous membrane was assumed to have a contact impedance of 20 $\Omega.cm^2$ based on independent measurements and the conductivity of the fluid was estimated to be 1.5 S/m. Total resistance was measured by dividing the difference in the average potential on each sense electrode ($V_+ - V_-$) by the total current between the current carrying electrodes.

Supplementary Fig. 14 shows the predicted resistance values versus tissue TEER values. The model predicts that the baseline subtracted (corrected) measured resistance correlates linearly with the tissue's contribution to the TEER value. Note the measured values are negative for low tissue TEER values and monotonically increase. By subtracting the baseline value before adding at tissue TEER, the curve is shifted to positive TEER values. The negative resistance values are explained as follows. The zero crossing occurs (approximately) when the tissue resistance is of the same magnitude as the channel resistance; when the tissue resistance is lower than the channel resistance, the current path goes through the initial tissue predominantly at the proximal tissue end (nearest the current source) causing the negative sense electrode to have a higher potential than the positive sense electrode. As the tissue dominates the overall resistance (high TEER values), the current moves through the tissue uniformly causing the positive sense electrode to have a higher potential than the negative sense electrode.

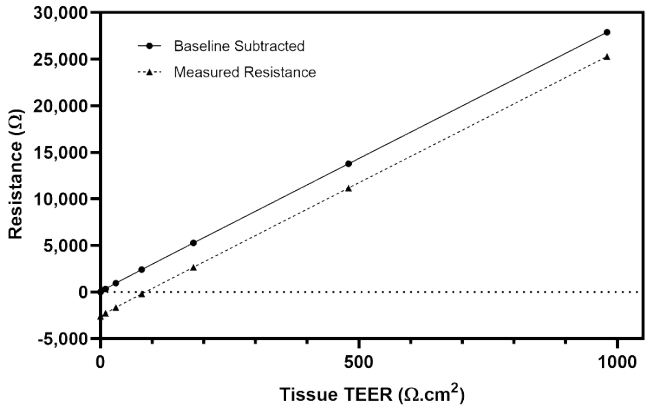

Supplementary Fig. 14 | Predicted total measured resistance versus tissue TEER values.

Supplementary Fig. 15 quantifies the current non-uniformity through the membrane as measured by the predicted normalized root mean square error of the square of the current through the membrane. Only at higher TEER values (e.g. > ~100 Ω) does the error become less than 10% of the mean.

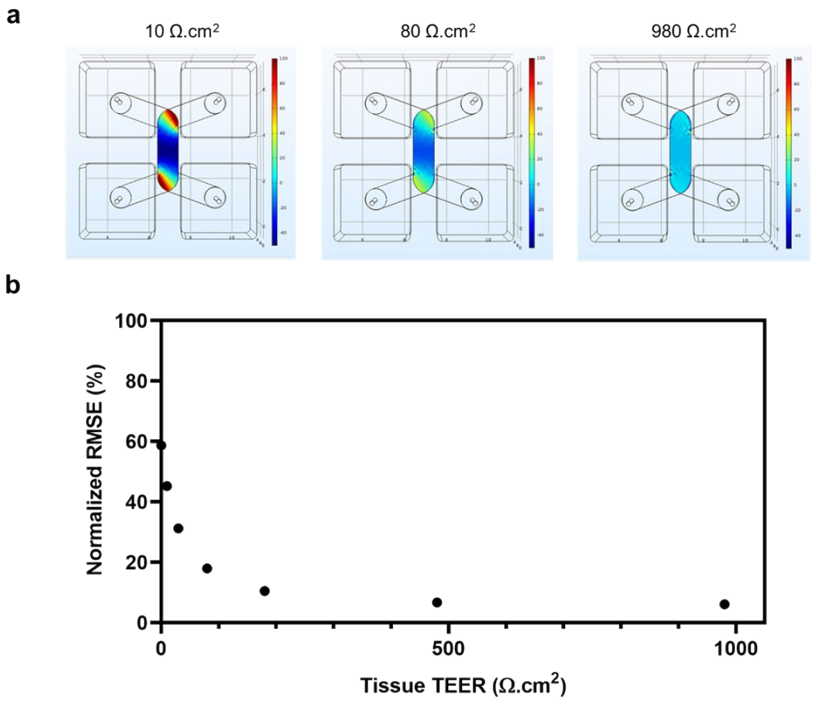

Supplementary Fig. 15 | Current uniformity. a, Heat map of current density normal to the membrane as a function of tissue TEER showing the predicted current density uniformity increases as a function of tissue TEER. Values are calculated by the difference of the square of the normal membrane current density minus the average normal membrane current density squared divided by the average normal current density squared multiplied by 100. **b**, Predicted current non-uniformity as measured by the normalized root mean square error of the square of the normal current density through the membrane.

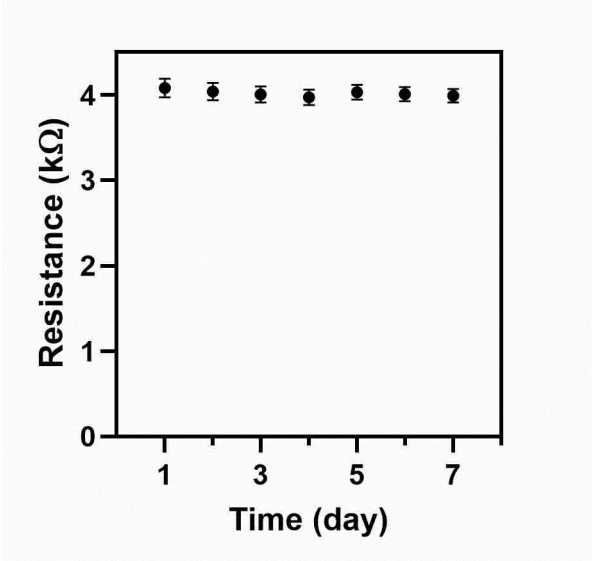

Supplementary Fig. 16 | Stainless steel electrode stability data as a function of time. To assess the stability of the stainless steel electrodes, resistance values were collected over a 7 day period using acellular devices (n = 4). Small

fluctuations are attributed to changes in temperature as these measurements were performed outside an incubator environment.

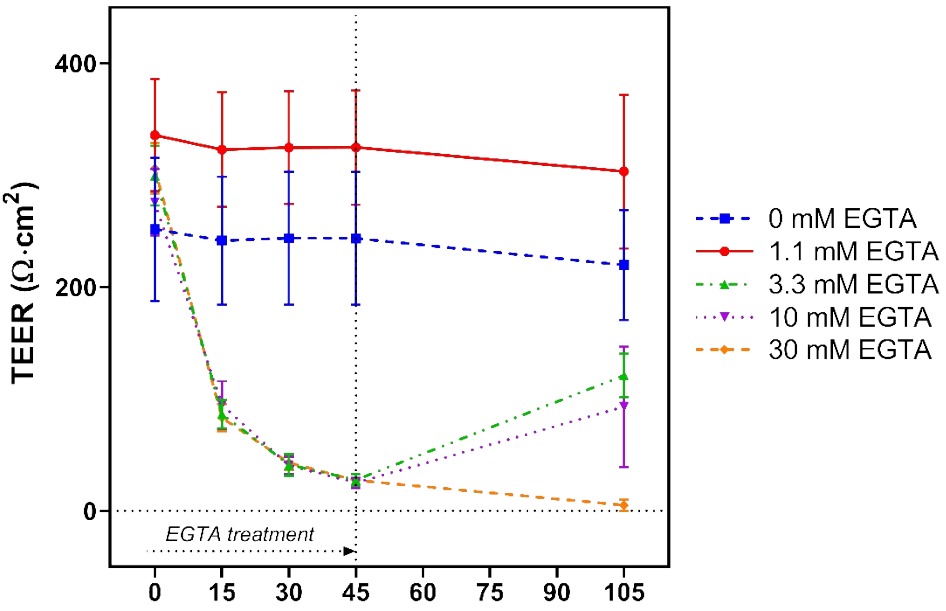

Supplementary Fig. 17 | Absolute TEER values samples over time of colon monolayers treated with EGTA. Absolute TEER values reported as Ω·cm² for primary intestinal colon monolayers treated with various doses of EGTA over 45 minutes, followed by wash out (dotted line) and 60 minute recovery period. Error bars represent standard deviation from the mean, n = 4 per group.

Model-specific Cell Suspension Preparation

PHH Suspension Preparation: Cryopreserved PHH (Lot HUM4075B: Lonza, Portsmouth, NH, USA) were seeded into cell culture plates as previously described(6). Briefly, after thaw and transfer to hepatocyte thaw media (MCHT50: Lonza), the cell suspension was gently mixed and centrifuged at 100 Xg for 7 minutes without brake. The suspension was re-suspended in hepatocyte plating media (MP250: Lonza) and re-centrifuged for another 7 minutes at 100 Xg. Cells were gently re-suspended in hepatocyte plating media at a density of 500,000 viable cells/mL, as assessed by Trypan blue stain (Thermo Fisher Scientific, Waltham, MA, USA). Viability of PHH before seeding by Trypan blue stain was 85% or higher.

Intestinal Spheroid dissociation: Colon cells were prepared for delivery into the devices following typical methods to dissociate spheroids(7–10). In brief, media was removed from spheroids in Matrigel (Lot. 6263007: Corning, Inc., Corning, NY, USA) domes in 24 well plates. Cells and Matrigel were collected by scraping Matrigel domes into 0.5mM EDTA in PBS. Matrigel and spheroids were centrifuged at 400g for 4 minutes. Pelleted cells were treated with 0.25% trypsin in 0.5mM EDTA in PBS for 4 minutes in 37 C water bath with intermittent mixing. Base medium, consisting of Advanced DMEM/F12, 20% fetal calf serum, 1X Penicillin/Streptomycin, 1 X GlutaMax, (all: Thermo Fisher Scientific, Waltham, MA, USA), was added to deactivate trypsin, and spheroids were triturated to obtain a suspension of small clumps of cells and single cells. The cell suspension was centrifuged at 400 Xg for 4 minutes. Following an additional wash in base medium and centrifugation, the cells were suspended at a concentration of 1 x 10^6 cells/mL for the EGTA barrier disruption experiment or 4 x 10^5 cells/mL for the proliferation versus differentiation experiment in expansion medium, developed according to previous literature (10,11).

Immunofluorescence Staining:

Experiment	Cell Type	Primary antibody	Dilution	Supplier	Catalog #
HCS assay	Human hepatic stellate cells Human retinal pericytes	α-smooth muscle actin (αSMA), clone 1A4	1:500	Millipore Sigma	A2547
		Collagen 1	1:1000	Abcam	ab6308
		Hoechst 33342	1:1000	Thermofisher	H3570
Vascular FSS	Retinal microvascular Ecs	CD31	1:250	Abcam	ab28364
		Hoechst 33342	1:1000	Thermofisher	H3570
Gut barrier function	Primary colon epithelial cells	ZO-1	1:200	Thermofisher	339100
		Hoechst 33342	1:1000	Thermofisher	H3570
Kidney oxygen sensing	Primary renal proximal tubule cells	Actin	1:500	Abcam	ab176758
		Hoechst 33342	1:1000	Thermofisher	H3570
Kidney transport	Primary renal proximal tubule cells	OAT-1	1:50	Thermofisher	PA5-26244
		Hoechst 33342	1:1000	Thermofisher	H3570

References

1. Mortensen NA, Okkels F, Bruus H. Reexamination of Hagen-Poiseuille flow: shape-dependence of the hydraulic resistance in microchannels. Phys Rev E. 2005 May 5;71(5):057301.

2. Berker R. Integration des équations du mouvement d'un fluide visqueux incompressible. Handbuch der Physik, Bd VIII/2, Encyclopedia of Physics. Berlin: Springer-Verlag; 1963.

3. Fuchs HU. Storage and Flow of Fluids and Electricity. In: Fuchs HU, editor. The Dynamics of Heat: A Unified Approach to Thermodynamics and Heat Transfer [Internet]. New York, NY: Springer; 2010 [cited 2020 Sep 13]. p. 17–50. (Graduate Texts in Physics). Available from: https://doi.org/10.1007/978-1-4419-7604-8_2

4. Yeste J, Illa X, Gutiérrez C, Solé M, Guimerà A, Villa R. Geometric correction factor for transepithelial electrical resistance measurements in transwell and microfluidic cell cultures. J Phys Appl Phys. 2016 Aug;49(37):375401.

5. Odijk M, Meer AD van der, Levner D, Kim HJ, Helm MW van der, Segerink LI, et al. Measuring direct current trans-epithelial electrical resistance in organ-on-a-chip microsystems. Lab Chip. 2015 Jan 22;15(3):745–52.

6. Tan K, Coppeta J, Azizgolshani H, Isenberg BC, Keegan PM, Cain BP, et al. Correction: A high-throughput microfluidic microphysiological system (PREDICT-96) to recapitulate hepatocyte function in dynamic, re-circulating flow conditions. Lab Chip. 2020 Aug 5;

7. Sato T, Vries RG, Snippert HJ, van de Wetering M, Barker N, Stange DE, et al. Single Lgr5 stem cells build crypt-villus structures in vitro without a mesenchymal niche. Nature. 2009 May;459(7244):262–5.

8. Jung P, Sato T, Merlos-Suárez A, Barriga FM, Iglesias M, Rossell D, et al. Isolation and in vitro expansion of human colonic stem cells. Nat Med. 2011 Oct;17(10):1225–7.

9. VanDussen KL, Marinshaw JM, Shaikh N, Miyoshi H, Moon C, Tarr PI, et al. Development of an enhanced human gastrointestinal epithelial culture system to facilitate patient-based assays. Gut. 2015 Jun;64(6):911–20.

10. Miyoshi H, Stappenbeck TS. In vitro expansion and genetic modification of gastrointestinal stem cells as organoids. Nat Protoc. 2013 Dec;8(12):2471–82.

11. Sato T, Stange DE, Ferrante M, Vries RGJ, van Es JH, van den Brink S, et al. Long-term Expansion of Epithelial Organoids From Human Colon, Adenoma, Adenocarcinoma, and Barrett's Epithelium. Gastroenterology. 2011 Nov;141(5):1762–72.